The Journal of Supercritical Fluids 228 (2026) 106785

Contents lists available at ScienceDirect

The Journal of Supercritical Fluids

journal homepage: www.elsevier.com/locate/supflu

The impact of processing conditions on PGSS micronisation of Fischer-Tropsch waxes

Andri Swanepoel [a,b], Philip W. Labuschagne [b], Cara E. Schwarz [a,*]

[a] Department of Chemical Engineering, Stellenbosch University, Banghoekweg, Stellenbosch 7600, South Africa
[b] Centre for Nanostructures and Advanced Materials, Council for Scientific and Industrial Research, Meiring Naude Road, Pretoria 0001, South Africa

HIGHLIGHTS

- PGSS micronisation of two Fischer-Tropsch waxes.
- Investigating the impact of pressure, temperature, wax loading and nozzle diameter.
- Interpret particle size, particle shape and bulk density results.
- Bimodal size distributions measured at low pressure and high wax loading.
- Monitoring impact of processing conditions on particle crystal structure.

GRAPHICAL ABSTRACT

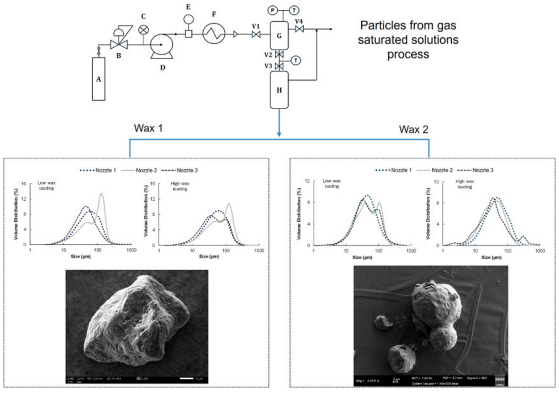

ARTICLE INFO

Keywords:
PGSS
Carbon dioxide
Wax
Particle size

ABSTRACT

Micronisation of two Fischer-Tropsch waxes with differing melting temperatures (Wax 1 <Wax 2) via the particles from gas saturated solutions process (PGSS) was successfully performed. The impact of pressure, temperature, wax loading and nozzle type on particle size, morphology and bulk density was investigated. Increased wax loading increased particle size and reduced sensitivity to changes in pressure and temperature. Nozzle diameter did not impact particle size greatly, but nozzle shape did. Bimodal particle size distributions were observed at low pressure and low temperatures. Wax 2 formed spherical, non-porous particles at low pressure and high temperature due to delayed solidification. Micronisation reduced lamellar size but had little effect on crystal structure. Wax 2 showed greater crystal stability over time than Wax 1. The results demonstrate that PGSS process parameters, particularly temperature and nozzle shape, influence wax particle characteristics, providing critical insights for optimising micronisation strategies in industrial applications.

* Corresponding author.
E-mail address: cschwarz@sun.ac.za (C.E. Schwarz).

https://doi.org/10.1016/j.supflu.2025.106785
Received 2 May 2025; Received in revised form 10 September 2025; Accepted 14 September 2025
Available online 19 September 2025

1. Introduction

Traditional methods to produce microparticles, including milling, spray chilling, spray drying and emulsification via solvent evaporation, require the use of high temperatures, high shear, the use of organic solvents and/or other harsh processing conditions [1]. Processes based on the use of supercritical fluids (SCF) for preparation of particles offer versatile alternatives to these more traditional methods. SCFs exhibit the density and solvent power of liquids, along with the enhanced diffusivity and reduced viscosity of a gas, and thus mass transfer can be greatly enhanced [2]. CO_2 is the most widely used SCF due to its relatively low critical temperature (31.1 °C), while also being non-flammable, non-toxic and easily separated from final product materials and low cost [3,4]. CO_2 is an extremely versatile and tuneable solvent, with significant variations in density possible with small changes in temperature and pressure in the vicinity of its critical point [1,5].

Of the different processes that rely on the use of SCFs for particle formation, the particles from gas saturated solution (PGSS) process [6] offers a simple and cost-effective approach to the production of microparticles. PGSS micronisation relies on the solubility of supercritical CO_2 (sc-CO_2) in a solute. The melting point and viscosity of the solute phase is reduced due to the presence of dissolved sc-CO_2 and spraying of the compound can thus be achieved [7]. The gas saturated liquid/solution is rapidly depressurised through a nozzle, and particles are formed and solidified due to supersaturation of the solution and rapid cooling via the Joule-Thompson effect. PGSS has been extensively studied for use in food [7–9] and pharmaceutical [10–12] applications, with the reduction in melting point in the presence of sc-CO_2 allowing for encapsulation of a wide range of thermosensitive compounds [13–19].

Various studies [16,20–24] have been performed to investigate how altering PGSS process parameters (pressure, temperature, solute loading and nozzle size) affect particle characteristics such as size, size distributions and morphology in many different single or multi-component systems. The use of PGSS for preparation of Fischer-Tropsch (FT) wax microparticles however has not yet been investigated.

Synthetic wax particles play an important role in various applications, providing scratch resistance and texture control to products such as paints, coatings and inks, with the size and shape (distributions) of the wax particles critical to product efficacy. FT waxes are synthesised via catalytic conversion of a CO/H_2 mixture via the FT process. The resultant mixture of hydrocarbons, oxygenates and water is further refined into a range of components, including commercial FT waxes [25]. FT waxes consist of linear saturated hydrocarbons with very limited branching and are produced consistently with high degrees of purity [26]. The FT process mainly utilises natural gas as feedstock, but there is growing interest in utilising organic waste or biomass as alternative carbon sources [27,28]. FT waxes thus offer a more sustainable alternative to other polyolefin based synthetic waxes, and if postprocessing can be achieved via a recognised green process such as PGSS it would further add to the environmentally friendly credentials of the final micronised product.

High pressure micronisation of synthetic waxes have been performed, but with the Rapid Expansion from Saturated Solutions (RESS) process [29,30]. The RESS process however requires that the solute be highly miscible in the SCF used, a factor that severely limits the compounds that can be micronised via sc-CO_2 as well as increasing SCF consumption. Alternative SCFs can be used, but these are often highly flammable and/or have much higher critical temperatures than CO_2, making them undesirable from a production point of view. PGSS micronisation in sc-CO_2 offers a more economical and safer alternative to the RESS process, especially for low value high volume products such as wax particles.

The current work aimed to successfully produce FT wax particles via PGSS, processing two waxes with increasing melting temperatures (T_m) (Wax 1 < Wax 2). Previously measured high-pressure phase boundaries and thermophysical properties of mixtures of these FT waxes and sc-CO_2 [31] was utilised to assist in investigating the interdependencies between PGSS processing conditions (temperature, pressure, composition and nozzle size) and the resulting FT wax particle size and shape. The work also aimed to determine the impact of PGSS processing on the crystal structure of the wax particles produced after micronisation over a six months period.

2. Materials and methods

2.1. Materials

The waxes used in this study were kindly provided by Cirebelle (Randburg, Gauteng, South Africa). Wax 1 (product code CB505) has an average T_m (at atmospheric pressure measured via DSC) of 40.1 °C and a molecular weight (M_w) of 457.5 g/mol, while Wax 2 (Product code CB303) displays an average T_m of 58.9 °C and a M_w of 546.1 g/mol, as measured previously [31]. High-pressure phase boundaries of binary mixtures of the two waxes with CO_2 indicated that Wax 1 behaved similar to published data on pure octacosane, while Wax 2 phase boundaries approximated that of pure C36 at similar mixture compositions and temperatures [31]. The densities of the mixtures of the two waxes at the phase boundary conditions, as well as the high-pressure viscosity of the binary mixtures of Wax 1 and CO_2 have been communicated previously [31]. CO_2 (purity of 99.99 %, product number K243C) was purchased form Air Products (Johannesburg, Gauteng, South Africa).

2.2. Wax particle production

The PGSS equipment utilised for micronisation was previously described [32], with a schematic of the equipment shown in Fig. 1. The system consists of a high-pressure mixing vessel mixing vessel (G) (500 mL internal volume), connected to a product chamber (H) (10 L internal volume) via a heated line (25 cm in length with an internal diameter of 4 mm). The mixing vessel is rated to a maximum pressure of 310 bar and at a maximum temperature of 150 °C. CO_2 is pumped to the mixing vessel via a Milton Roy Dosapro membrane pump (D). The pressure in the mixing vessel is regulated by a back pressure valve, and the pressure is measured by an Ashcroft pressure sensor. CO_2 flow is measured by a Rheonik (Odelzhausen, Bavaria, Germany) flow meter. Temperature in the mixing vessel is measured by a 3 wire PT100 sensor.

The waxes were loaded into the pre-heated mixing vessel and the mixing vessel sealed. The mixing vessel was pressurised to approximately 30 bar using pressure from the CO_2 cylinder and then vented until the pressure reached approximately 10 bar, in order to flush atmospheric air from the mixing vessel. The mixing vessel was then pressurised to the required set point pressure utilising the membrane pump, and the CO_2-wax mixture was allowed to equilibrate for 1 hr. This residence time was informed by previous studies [20,22] as well as practical implications. Valve V2 in Fig. 1 was opened with the melt/-solution filling the heated line connecting the mixing vessel and the product chamber. Valve V3 (Fig. 1) was opened and closed manually three times, at ± 2 s intervals, to facilitate expansion of the molten material into the product chamber. The spraying time was kept brief to prevent pressure in the mixing vessel reducing drastically, and thus the stability of the flow generated during spraying may have been compromised. Thereafter 5 min were allowed for conditions in the product chamber to stabilise before performing another set of sprays. For the lower wax loading 5 sets of sprays were performed, and for the higher wax loading 10 sets, with total spraying time varying between 30 min to 1 hr. The melt was sprayed through a heated nozzle (set at 100 °C to prevent blocking of the nozzle) into the product chamber maintained at atmospheric pressure and room temperature (maintained at 20 °C via air conditioning). The experimental procedure was applied consistently at all conditions while utilising three different nozzles.

Three different nozzle sizes were utilised and referred to as Nozzle 1,

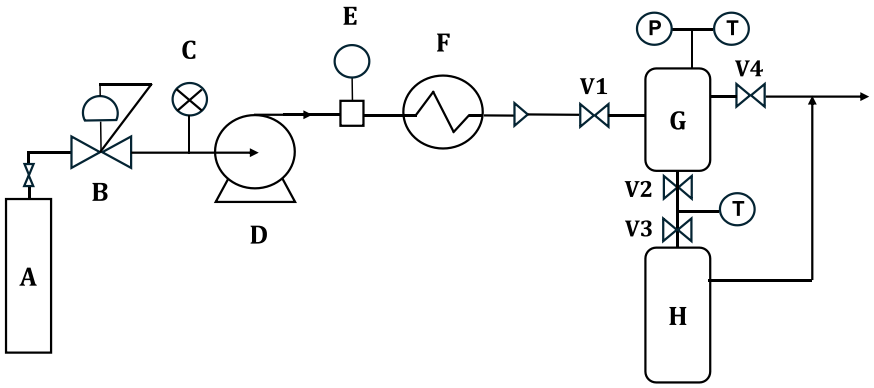

Fig. 1. Schematic representation of the PGSS process, with A) CO_2 cylinder, B) back pressure regulator, C) pressure gauge, D) diaphragm pump, E) flow meter, F) CO_2 pre-heater, G) mixing vessel and H) product chamber.

Nozzle 2 and Nozzle 3. Nozzle 2 is a semi-tapered nozzle supplied by Separex (Nancy, Lorraine, France). Nozzles 1 and 3 have uniform diameters that were manufactured in-house. A schematic representation along with the dimensions of the nozzles are shown in Fig. 2. Initial experiments with a smaller nozzle (diameter of 0.5 mm) resulted in severe blockages of the nozzle, and hence nozzles of 1 mm diameter or greater were used for the experiments. Improvements to the nozzle heater capacity and efficiency could possibly resolve this issue.

The processing parameters altered during the project included the temperature and pressure in the mixing vessel, the mass of wax loaded, and the spraying nozzle utilised. The temperatures and pressures used for micronisation were informed by the melting and phase behaviour of the waxes in sc-CO_2 conducted previously [31]. Wax 1 was micronised at 35 °C, 40 °C, 45 °C and 50 °C, and at 100 bar, 150 bar, 200 bar and 250 bar, while Wax 2 was micronised at 60 °C, 70 °C, 80 °C and 90 °C, at 100 bar, 200 bar and 300 bar.

The impact of mass loading was investigated qualitatively by investigating the difference in particle characteristics when micronising with two different masses of wax loaded to the pressure vessel. The higher wax loading experiments were performed with the maximum mass of wax that could be safely processed with the equipment. For Wax 1 this amounted to 160 g of wax per experiment, and 210 g of Wax 2 per experiment, kept constant at all processing conditions [33], and referred to as x_{wax_high}. Experiments were repeated with a decreased wax loading of 100 g (for both Wax 1 and Wax 2), referred to as x_{wax_low}.

Production yield was determined by weighing the mass of free-flowing powder produced at the different processing conditions. At instances where wax remained in the mixing vessel, the content of the mixing vessel was also weighed. Significant aggregates in the product chamber as well as particles on the underside of the lid of product chamber were also weighed but not included in the mass yield reported. Any mass of wax still unaccounted for was attributed to losses in the lines of the equipment and possible venting of a fraction of smaller particles.

The repeatability of the process was tested by repeating experiments at selected conditions twice, with an average variation of 1.8 % in median particle size obtained between the three runs.

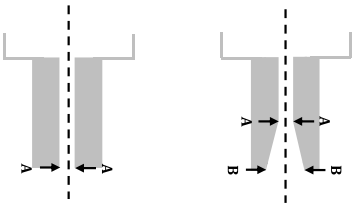

	A	B
Nozzle 1	1 mm	
Nozzle 2	2.4 mm	5.25 mm
Nozzle 3	3 mm	

Fig. 2. Schematic representation of the three nozzles used for micronisation.

2.3. Particle size measurement

Particle size was measured via laser diffraction (according to ISO 13320) with a Microtrac Sync particle analyser (Verder Scientific, Haan, North Rhine-Westphalia, Germany) that utilises a modified Mie scattering theory to determine particle size. Precision of the laser diffraction measurements is given as 1.0 %.

Approximately 50 mg of wax powder was added to 20 mL of deionised water. Non-ionic surfactant (domestic rinse aid) (25 µl) was added to the suspension to disperse the hydrophobic wax particles in the water. The sample was magnetically stirred for 15 min at 300 rpm. For every experimental point, three to four samples were prepared in this manner and analysed via laser diffraction. The refractive indices used for water and the waxes were 1.33 and 1.50 respectively. A statistical composite of the different runs was created by the equipment software, and the resultant particle size distribution (PSD) determined. Particle size was chiefly investigated according to the D10, D50 (median) and D90 values of the distributions, i.e. the diameters where 10 %, 50 % and 90 % respectively of the particles in the cumulative volume distribution are smaller than these values. Where PSDs were classified as multimodal by the laser diffraction software, single D10, D50 and D90 values per PSD were calculated as the weighted averages of the parameters of the separate peaks by the software. Statistical analysis of particle size data was performed via 2 sample t-tests at a 95 % confidence interval.

2.4. Particle shape

The Sync particle analyser utilised to determine particle size is also fitted with dynamic image analysis (ISO 13322–2) capabilities that can quantitively measure and calculate a large variety of shape parameters, simultaneously to size measurements. For the purposes of this study, data regarding circularity, width to length (WL) aspect ratio and transparency were obtained. Circularity is a measure of how close the particle shape approximates that of a perfect smooth sphere, with measurements ranging between 0 and 1, where 1 is a perfect sphere. Circularity is calculated according to Eq. 1 by the equipment software.

$$Circularity = \frac{4\pi \times \text{Area}}{Perimeter^2} \quad (1)$$

The WL aspect ratio is also a measure of roundness of a particle and is determined as the ratio between the width and the length of the particle, as shown in Eq. 2.

$$WL\ aspect\ ratio = \frac{Width}{Length} \quad (2)$$

Transparency is determined as the mean light intensity of the longest vertical line analysed per particle. Measurements range between 0 and 1, with the least transparent particles measuring 0, and the most

transparent particles measuring 1.

The particle shape analyses performed via dynamic imaging was complimented by SEM imaging to visually inspect wax particle shape. Due to the relatively low T_m of Wax 1, particles could not be carbon coated and imaged in a high vacuum environment. Wax 1 particles were coated via vapour deposition with a 1 % osmium solution overnight at 4 °C and imaged with a JEOL IT200 (Japan) at 3 kV to 5 kV in low vacuum mode. Wax 2 particles were carbon coated twice for 30 s each and visualised with a Zeiss Auriga SEM (Germany) with a field emission gun and EDX detector (Oxford X-max with Aztec software).

2.5. Bulk density

Bulk density was determined according to a previously published method [16,19,34]. A 50 mL pre-weighed glass beaker was filled evenly with micronised wax and weighed. The density of the powder was then determined as the weight of the wax divided by the volume of the beaker. Measurements were performed with minimal disturbance to the wax particles in the glass beaker to prevent compacting from impacting the results. Measurements were performed in triplicate at least.

Tapped densities were also determined, with between 4 g and 6 g of wax powder added to a measuring cylinder. The cylinder was tapped until no further changes in volume were observed, and the tapped density determined as the weight of the wax particles divided by the final volume noted.

2.6. Thermal behaviour

Thermal analyses of the wax materials were performed using a differential scanning calorimeter (DSC Q2000, TA Instruments, New Castle, Delaware, USA). Samples of between 0.5 mg and 2 mg were prepared in aluminium sample pans and analysed in a nitrogen atmosphere maintained at a flow rate of 10 mL/min. Heating and cooling were performed at 10 °C/min between −30 °C and 200 °C. The average ambient T_m and the enthalpy of melting (ΔH_m) were determined from the results. The results for T_m and ΔH_m were obtained from the first heating cycle to best represent the exact heating behaviour of the reference as well as micronised wax samples [35].

2.7. Crystal structure

The crystal structures of the micronised particles were monitored via X-ray diffraction (XRD). XRD patterns were obtained via a Malvern PANalytical X'Pert Pro XRD equipment (Almelo, The Netherlands), with a Cu Kα radiation source (λ =1.5406 Å). Analyses were performed at a filament intensity of 40 mA and a voltage of 45 kV. Two sets of divergence and anti-scatter slits were utilised to accurately determine scattering from lower angle and higher angle regions, namely 1/32° and 1/16°, and 1/4° and 1/2°. Samples were stored at 4 °C after micronisation until XRD analyses could be performed.

The stability of the crystal structures and melting points of the micronised wax particles were monitored over a six month period. Samples were stored in a humidity chamber at 25 °C and at 50 % relative humidity, with XRD and DSC analyses performed after 1 month, 3 months and 6 months in duplicate.

3. Results

3.1. Mass yield and ease of processing

PGSS micronisation of Wax 1 could be performed with varying degrees of mass yield of free-flowing powder between 100 bar and 200 bar (as shown in Table 1).

* Experiments performed with virtually no yield produced due to pressure induced crystallisation

At 200 bar and 250 bar at lower temperatures, and at 250 bar at higher temperatures, very little to no free-flowing wax powder was produced. This can be attributed to changes in viscosity and heat transfer rates, as follows. At low temperature, viscosity is increased [31], hindering flow of the wax-CO_2 melt from the mixing vessel to the product chamber, and thus adversely affecting yield. As pressure is increased at 35 °C and 40 °C, pressure-induced crystallisation occurs in the mixing vessel [31] resulting in reduced mass yield with very little material flowing to the product chamber. Above 150 bar the pressure induced crystallisation occurs to such an extent that micronisation cannot occur at all. As temperature is increased to 45 °C and 50 °C, yield improves due to a reduction in viscosity and improved material flow, with micronisation at 200 bar resulting in improved mass yield. Above 200 bar micronisation could not be performed successfully at any of the experimental temperatures.

At higher temperatures, the rate of heat transfer required for the formation of solid particles in the product chamber increases. At lower pressure, less CO_2 is dissolved in the wax melt [31], and less energy is required for evaporation of the CO_2 during expansion. Less heat is thus

Table 1
Mass yield (%) of free-flowing powder produced via PGSS micronisation of Wax 1.

T (°C)	P (bar)	Nozzle 1		Nozzle 2		Nozzle 3	
		x_{wax_low}	x_{wax_high}	x_{wax_low}	x_{wax_high}	x_{wax_low}	x_{wax_high}
35	100	41[a]	43[a]	55[a]	58[a]	43[a]	57[a]
	150	32[a]	35[a]	41[a]	64[a]	65[a]	40[a]
	200	Not determined*					
	250	Not determined*					
40	100	93	96	76[b]	73[b]	53[b]	62[b]
	150	86[a]	89[a]	81[a]	74[a]	85[a]	93[a]
	200	Not determined*					
	250	Not determined*					
45	100	94	67[b]	83[b]	76[b]	68[b]	64[b]
	150	89	92	88	94	93	95
	200	89	89	85	90	90	93
	250	Not determined*					
50	100	59[b]	48[b]	71[b]	69[b]	43[b]	60[b]
	150	90	74[b]	92	95	85	86
	200	86	88	86	91	88	93
	250	Not determined*					

[a] Mass yield impacted by material not moving through to the product chamber
[b] Mass yield impacted by agglomeration/aggregate formation in the product chamber

removed from the molten wax during spraying. Therefore, at high temperatures and low pressures, agglomeration occurs in the product chamber due to incomplete solidification of discreet particles. This is compounded by an increase in wax loading. At lower temperatures and higher pressures yield is not greatly impacted by wax loading.

Increasing pressure results in greater cooling as more CO_2 evaporates during expansion. The rate of heat transfer is thus increased, and the formation of discreet particles (and an increased mass yield) is promoted.

The mass yields of free-flowing Wax 2 particles obtained are shown in Table 2. Micronisation of Wax 2 could be performed between 100 bar 300 bar and between 60 °C and 90 °C, with mass yield increasing with increasing temperature and pressure.

As with Wax 1, at low pressure and low temperature, high wax melt viscosity results in insufficient break-up of the solution into discreet particles. At low pressure and high temperature, agglomeration occurs due to unmet rates of heat transfer required for solidification of discreet particles. This is exasperated by an increase in nozzle diameter and a subsequent decrease in spraying velocity and reduced shear, resulting in very low to no mass yields produced at 100 bar/80 °C and 100 bar/90 °C with Nozzle 3. Nozzle 1 generally produced the greatest mass yields across all processing conditions, with yield not greatly impacted by wax loading. For Nozzle 2 and Nozzle 3, increased wax loading resulted in increased mass yield at low pressures, although mass yields at 100 bar for both nozzles are generally poor.

3.2. Particle size

3.2.1. Impact of wax loading on particle size

The PSD parameters D10, D50 and D90 measured for Wax 1 particles and Wax 2 particles are shown in Table 3 and Table 4, respectively. Bimodal PSD parameters are indicated via asterisk in both tables. For both waxes median particle size tends to increase with an increase in wax mass loading, especially when using Nozzle 2 As wax mass loading is increased, the viscosity of the wax melt increases [31] and break-up of the melt during depressurisation is less efficient, resulting in the formation of larger particles [24].

3.2.2. Impact of temperature, pressure and nozzle diameter on particle size

Comparison of the PSDs of Wax 1 particles prepared with Nozzle 2 at x_{wax_low} and at low pressure at various temperatures (Fig. 3a & b) shows that an increase in temperature results in a reduction in particle size due to a reduction in viscosity, with the peak maxima shifting to the left. As temperature is further increased the peak maxima tend to shift to the right again as the impact of particle agglomeration dominates over the impact of reduced viscosity. A similar trend was observed for Nozzle 1 PSDs (Figure S1 in Supplementary Material).

The impact of temperature on the PSDs is mitigated by an increase in Wax 1 loading for both Nozzles 2 and 1 (Fig. 3c & d and Figure S1 c & d). As wax loading is increased, viscosity increases to such an extent that changes in temperature do not impact viscosity and thus particle formation sufficiently to reflect in the resulting PSDs. The previous viscosity measurements of Wax 1 + CO_2 [31] indicated that at high pressures and at high temperatures viscosity is not impacted by increases in temperature and pressure to the same degree as at lower pressures and temperatures. This is reflected in the minimal variation in the D10, D50 and D90 values recorded at 200 bar/50 °C between Wax 1 particles prepared at x_{wax_low} and at x_{wax_high}, for both Nozzles 1 and 3.

The median diameters of Wax 2 particles produced with Nozzle 1 vary minimally with changes in temperature and pressure and even less when the wax loading is increased. Nozzle 3 median particle sizes also remained relatively constant, with a few exceptions.

At x_{wax_low}, at 100 bar and low temperatures, for both Nozzles 2 and 3, Wax 2 median particle sizes tended to be very similar and smaller than at other processing conditions. This can be ascribed to the lower yields at these conditions, with larger particles present in the large solid aggregates formed in the product chamber and smaller particles making up the free-flowing powder analysed. At 100 bar/90 °C, larger median particle sizes are indicative of greater agglomeration, and the PSD shifts more to the right (Figure S2 a in Supplementary Material). As pressure is increased to 300 bar and mass yield is improved, the impact of temperature on particle size is reduced (Figure S2 b).

At x_{wax_high}, where mass yields are greater and more representative, particle size is not greatly impacted by changes in pressure and temperature. This supports the conclusion that changes in Wax 2 particle size with temperature and pressure at x_{wax_low} are impacted largely by sub optimal mass yield.

The PSDs of Wax 1 particles prepared with Nozzle 1 and Nozzle 3 were overwhelmingly classified as unimodal by the laser diffraction software. PSDs produced with Nozzle 2 however showed much more bimodality, with most of the PSDs produced at x_{wax_high} classified as bimodal, as illustrated in Fig. 3. The high prevalence of bimodality within Nozzle 2 PSDs explains why the (weighted average) D50 values of Wax 1 particles at x_{wax_high} (Table 3) are thus also generally much higher than those produced at x_{wax_low}, and also much greater than the D50 values produced by Nozzles 1 and 3 under similar processing conditions.

Multimodal distributions of PGSS produced particles (of fully hydrogenated soybean oil) have been previously documented [22]. The authors postulated that the fluid passing through the spraying nozzle consisted of two distinct parts, with an outer layer (in contact with the

Table 2
Mass yield (%) of free-flowing powder produced via PGSS micronisation of Wax 2.

T (°C)	P (bar)	Nozzle 1		Nozzle 2		Nozzle 3	
		x_{wax_low}	x_{wax_high}	x_{wax_low}	x_{wax_high}	x_{wax_low}	x_{wax_high}
60	100	95	97	26	71	66	58
	200	91	92	92	65	81	88
	300	74[a]	67[a]	54[a]	88	80	87
70	100	98	94	35[b]	66	72	81
	200	94	97	92	78	90	89
	300	88	89	87	94	84	92
80	100	88	94	39[b]	72	0[b]	58[b]
	200	95	91	92	97	91	90
	300	90	93	89	92	88	93
90	100	79	77	30[b]	70	0[b]	43[b]
	200	93	96	91	97	94	90
	300	93	95	90	97	88	94

[a] Mass yield impacted by material not moving through to the product chamber
[b] Mass yield impacted by agglomeration/aggregate formation in the product chamber

Table 3
The distribution parameters of Wax 1 particles micronised with three different nozzle sizes at lower (x_{wax_low}) and higher (x_{wax_high}) wax mass loadings.

	T (°C)	P (bar)	x_{wax_low} Diameter (μm)			x_{wax_high} Diameter (μm)		
			D10	D50	D90	D10	D50	D90
Nozzle 1	35	100	14	46 ± 3.6	109	17	48 ± 2.0	114
		150	14	45 ± 3.7	122	17	51 ± 2.9	119
	40	100	16	51 ± 3.7	116	15	46 ± 3.9	114
		150	15	45 ± 1.9	134	17	50 ± 5.3	120
	45	100	13	43 ± 4.7	111	16	52 ± 2.9	122
		150	15	45 ± 5.2	110	15	46 ± 4.8	112
		200	17	47 ± 1.4	124	15	44 ± 1.4	112
	50	100	15	46 ± 2.8	138	17	47 ± 5.3	120
		150	17	56 ± 3.5	138	16	47 ± 5.1	112
		200	17	49 ± 2.5	128	17	49 ± 19*	124
Nozzle 2	35	100	18	75 ± 33	157	23	94 ± 24*	213
		150	12	44 ± 18*	133	19	80 ± 34*	156
	40	100	17	55 ± 18*	123	15	67 ± 28*	153
		150	13	38 ± 5.2	99	19	77 ± 19*	145
	45	100	11	37 ± 9.6	105	17	71 ± 20*	126
		150	10	31 ± 1.6	80	19	85 ± 16*	158
		200	15	47 ± 11	129	26	91 ± 27	166
	50	100	13	45 ± 3.0	106	14	55 ± 32*	142
		150	12	38 ± 22*	108	17	66 ± 22*	147
		200	14	49 ± 17*	120	22	91 ± 10	239
Nozzle 3	35	100	13	39 ± 9.0	102	14	44 ± 2.9	110
		150	14	46 ± 6.0	108	15	48 ± 6.1	122
	40	100	14	42 ± 3.7	111	16	50 ± 5.0	118
		150	16	51 ± 6.8	117	12	43 ± 17	127
	45	100	14	48 ± 3.0	115	15	42 ± 3.5	106
		150	15	45 ± 4.0	122	14	41 ± 1.5	114
		200	15	46 ± 3.8	111	17	50 ± 2.1	122
	50	100	13	40 ± 2.3	108	16	51 ± 3.8	118
		150	16	47 ± 4.4	116	17	54 ± 3.1	118
		200	15	44 ± 3.4	114	14	43 ± 1.5	108

* Bimodal distributions

inside nozzle wall) consisting of solute solution saturated in CO_2, and an inner part consisting of entrained solute and CO_2 saturated in solute [22]. It was hypothesised that in the outer layer particle formation occurred via atomisation and expansion, while crystallisation was identified as the mechanism for particle formation in the inner layer [36]. During expansion the outer layer increases in volume, and the two layers intermingle, resulting in a mixture of atomised and crystallised particles that adhere to each other due to differences in size. It was concluded that particles formed via these different mechanisms (atomisation, crystallisation and varying degrees of agglomeration) resulted in PSDs with multiple peaks [22].

Comparison of the peak maxima and volume fractions that each peak in the Nozzle 2 bimodal distributions occupy (Table 5) indicates that the median particle sizes of the second peaks (i.e. the set of smaller particles in the distribution) are smaller than the median particle sizes of the other unimodal distributions.

The fractions of smaller particles can be ascribed to atomisation occurring in the outer layer consisting of wax saturated in CO_2. When micronising Wax 1 with Nozzle 2 at higher wax loading and lower pressures, mixing of the outer layer with the inner layer is minimised (due to reduced CO_2 expansion), and a separate set of smaller particle sizes per PSD is produced, resulting in bimodal PSDs. The higher wax loading combined with the tapered nature of Nozzle 2 however also enhances agglomeration of larger particles formed mainly via crystallisation in the inner layer. Agglomeration of particles can also occur in the period before stable flow through the nozzle is achieved.

At lower wax loading and high temperatures, bimodality occurs due to an increase in the relative proportion of the CO_2-rich outer layer. Even though more intermixing between the inner and the outer layers may occur, sufficient quantities of smaller particles are formed from the increased outer layer to constitute a separate set of particles, with this set representing more than half of the PSDs by volume. Larger particles are formed due to coalescence of partly solidified particles. At lower pressures and low temperatures, the expansion of the outer layer is reduced, while the inner solute rich layer is not ruptured efficiently into smaller particles due to higher viscosity. This results in the formation of two sets of particles with separate median sizes.

As with Wax 1, Wax 2 particle distributions prepared with Nozzle 1 showed minimal bimodality. Wax 2 particles prepared with Nozzle 2 and Nozzle 3 at x_{wax_high} at 100 bar also produced bimodal distributions due to reduced CO_2 expansion. These distributions become unimodal with increases in pressure, as illustrated in Fig. 4(a & b), due to greater expansion and thus mixing of particles from the inner and outer melt layers. The degree of bimodality also generally decreases with increases in temperature, with the proportion of larger particles reduced due to improved rupturing of the inner layer. This is illustrated by a reduction in the weighting of the set of larger particles in the PSD (Table 6).

Bimodal distributions were also observed at 200 bar/80 °C and at 300 bar/60 °C (Nozzle 2) and at high pressure and temperature (x_{wax_low}) and at 200 bar/90 °C (x_{wax_high}) when utilising Nozzle 3. As with Wax 1, the median sizes of the second peaks in the bimodal distributions are smaller than the D50 values of the unimodal distributions (Table 6). Nozzle 3 bimodal distributions at x_{wax_low} showed only slight bimodality at high pressure and temperature (due to agglomeration), with the weighting of the larger median peak much reduced as compared to the smaller median peak. As a result, the total D50 as determined by the laser diffraction software is not greatly impacted by the bimodality of the PSDs.

The bimodal PSD produced by Nozzle 2 at 300 bar/60 °C showed an increased D50 value for the second peak relative to the other bimodal distributions due to larger particles forming during atomisation at higher pressure (greater CO_2 expansion). However, at 60 °C the viscosity of the inner wax rich layer is still sufficiently high to prevent expansion to occur to the degree where mixing of the two layers will take place, and a bimodal distribution is produced.

The model can also be applied to explain the differences in mass yield

Table 4
The size distribution parameters of Wax 2 particles micronised with three different nozzle sizes at lower (x_{wax_low}) and higher (x_{wax_high}) wax loading.

	T (°C)	P (bar)	x_{wax_low}			x_{wax_high}		
			Diameter (μm)			Diameter (μm)		
			D10	D50	D90	D10	D50	D90
Nozzle 1	60	100	12	33 ± 4.4	87	14	38 ± 3.5	92
		200	14	38 ± 4.0	86	15	39 ± 3.1	87
		300	13	36 ± 2.8	98	17	41 ± 3.3	84
	70	100	14	37 ± 4.4	93	14	38 ± 4.1	93
		200	14	39 ± 3.1	102	14	37 ± 2.5	85
		300	13	39 ± 4.7	105	16	38 ± 4.8	84
	80	100	13	38 ± 4.1	103	13	39 ± 2.4	113
		200	12	34 ± 2.1	81	14	39 ± 2.0	89
		300	13	34 ± 6.2	87	16	39 ± 3.5	94
	90	100	14	40 ± 4.2*	127	15	42 ± 5.5	108
		200	12	35 ± 6.0	96	16	39 ± 4.8	91
		300	13	36 ± 2.4	91	16	40 ± 2.4	108
Nozzle 2	60	100	12	32 ± 7.0	75	13	39 ± 19*	105
		200	15	44 ± 5.1	106	15	41 ± 4.6	100
		300	18	47 ± 3.3	113	24	66 ± 28*	157
	70	100	11	33 ± 4.3	85	13	40 ± 15*	111
		200	11	37 ± 5.5	100	12	38 ± 2.9	100
		300	15	42 ± 3.0	104	13	38 ± 6.2	107
	80	100	14	46 ± 6.9	131	11	38 ± 13*	109
		200	16	43 ± 6.3	105	12	35 ± 14*	103
		300	13	40 ± 3.6	95	13	38 ± 5.9	83
	90	100	18	52 ± 6.9	115	11	33 ± 2.6	82
		200	12	40 ± 11	117	13	36 ± 5.3	83
		300	17	42 ± 1.8	91	11	31 ± 2.3	89
Nozzle 3	60	100	9	28 ± 5.0	69	14	38 ± 2.5	91
		200	17	49 ± 6.3	117	15	39 ± 1.5	89
		300	19	50 ± 6.7	115	18	45 ± 1.4	107
	70	100	7	28 ± 4.9	79	14	38 ± 4.6*	110
		200	12	37 ± 5.5	99	14	39 ± 3.5	95
		300	13	37 ± 2.4	88	15	41 ± 2.8	100
	80	100	Not determined#			12	41 ± 3.2*	113
		200	10	30 ± 3.3	81	14	38 ± 2.6	95
		300	14	42 ± 2.8*	121	15	37 ± 1.9	94
	90	100	Not determined#			9	31± 7.6*	114
		200	14	37 ± 8.5	93	12	39 ± 7.3*	113
		300	13	38 ± 3.2*	122	14	38 ± 3.9	107

#Parameters not determined due to insufficient yield
* Bimodal distributions

between x_{wax_low} and x_{wax_high} observed at certain low pressure conditions in Table 2. The greater CO_2 content at x_{wax_low} resulted in increased expansion and mixing of the smaller outer layer particles with the insufficiently ruptured inner melt layer. This results in increased agglomeration and generally a reduced mass yield at lower wax loadings. When micronising with Nozzle 3 at x_{wax_low} at 100 bar/80 °C and 90 °C agglomeration occurred to such an extent that a coating of wax was formed in the product chamber instead of discreet particles.

At higher wax loading differences in shape (and also PSD parameter values) between Wax 1 PSDs produced by Nozzle 2 compared to Nozzles 1 and 3 are evident when compared directly (Fig. 5), while these variations are reduced with increasing temperature.

An increase in nozzle diameter has been shown to result in an increase in median particle size due to decreased shear applied during micronisation [21]. When comparing Wax 1 particles produced with Nozzles 1 and 3, with similar geometry but different size, particle size does not increase consistently with increasing nozzle diameter. The difference in geometry between Nozzle 2 and Nozzles 1 and 3 thus plays a more significant role in Wax 1 median particle size and distribution shape than nozzle diameter, especially at higher wax loading.

The differences in Wax 2 PSDs produced by the three nozzles are less distinct than for Wax 1. Very little variation is observed when processing at the lower wax loading, with greater disparity between the PSDs of the three nozzles at higher wax loading, lower temperature and low pressure (100 bar), as shown in Fig. 6. This is mainly due to the bimodal distributions produced by Nozzles 2 and 3 at these conditions. The smaller diameter of Nozzle 1 results in increased spraying velocity, and more efficient rupturing of especially the inner layer in the nozzle. Smaller particles are thus formed via crystallisation that are indistinguishable from the particles formed via atomisation.

3.2.3. *Impact of wax melting point*

The tapered shape of Nozzle 2 impacts particle size and distribution shape less for Wax 2 than for Wax 1. This can be attributed to the greater liquid hydrocarbon fraction of Wax 1 versus the higher melting point Wax 2. During micronisation, expansion into the product chamber results in supersaturation, with the lightest fractions of wax falling out of solution last, coating the already formed particles [29]. The greater liquid hydrocarbon fraction of the lower T_m Wax 1 versus Wax 2 results in greater coating and thus a higher probability of particle agglomeration, with agglomeration compounded by the tapered section of Nozzle 2.

Nozzle 3 produced bimodal distributions for Wax 2 particles at low pressure and higher wax loading, but not for Wax 1 particles. Owing to its lower melting temperature, Wax 1 is processed at lower temperatures, conditions that provide higher CO_2 density and thereby enhance its solubility in the wax [31]. The greater CO_2 content thus results in improved cooling and sufficiently reduced levels of agglomeration to prevent the formation of a separate set of larger particles.

Even though the viscosity of Wax 2 could not be measured previously [31], it is reasonable to assume that the viscosity of Wax 2 melts will be greater than those of the lower M_w Wax 1 [37]. The decreased viscosity of Wax 1 and the resultant improved rupturing of especially the inner layer of material thus also contributes to the lack of bimodality observed

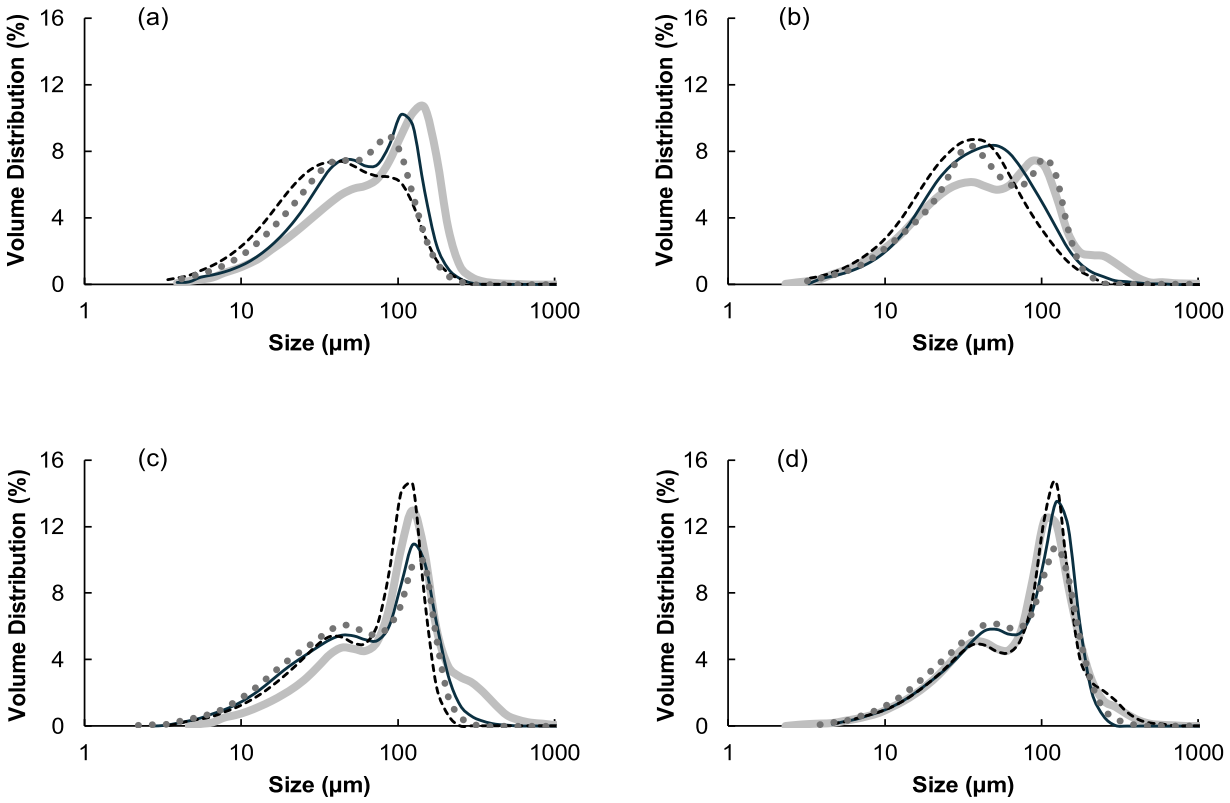

Fig. 3. PSD of Wax 1 particles prepared at 35 °C (thick solid line), at 40 °C (thin solid line), at 45 °C (dashed line) and at 50 °C (dotted line) with Nozzle 2 at a) 100 bar x_{wax_low}, b) 150 bar x_{wax_low}, c) 100 bar x_{wax_high} and d) 150 bar x_{wax_high}.

Table 5
Peak values of bimodal distributions of Wax 1 particles produced by Nozzle 2.

T (°C)	P (bar)	x_{wax_low}				x_{wax_high}			
		1st Peak (µm)	Vol (x/x)	2nd Peak (µm)	Vol (x/x)	1st Peak (µm)	Vol (x/x)	2nd Peak (µm)	Vol (x/x)
35	100	75	1.0	-	-	113	0.75	27	0.25
	150	86	0.50	21	0.50	102	0.69	25	0.31
40	100	93	0.52	29	0.48	111	0.57	26	0.43
	150	38	1.0	-	-	109	0.63	29	0.37
45	100	37	1.0	-	-	96	0.65	24	0.35
	150	31	1.0	-	-	105	0.70	25	0.30
	200	47	1.0	-	-	91	1.0	-	-
50	100	45	1.0	-	-	108	0.52	25	0.48
	150	89	0.38	26	0.62	106	0.57	28	0.43
	200	93	0.48	27	0.52	91	1.0	-	-

for Wax 1 particles prepared with Nozzle 3 versus Wax 2 particles prepared with Nozzle 3.

3.3. Particle shape

3.3.1. Wax 1 particle morphology via SEM

High resolution SEM imaging of Wax 1 proved challenging due to the low vacuum mode that had to be employed to prevent the particles from melting. SEM images of Wax 1 particles indicated that particles are generally spherical and smooth (Fig. 7a and b).

Limited porosity is observed at 150 bar and 200 bar, as shown in Fig. 7c, while larger particulate structures made up of smaller spherical particles fused together are also present (Fig. 7d). Very little variation in shape is observed in particles produced at different processing conditions with different nozzles, with samples generally displaying a mixture of morphologies present (Fig. 7e). The presence of more spherical particles (Fig. 7a and b) as well as structures with flat surfaces as shown in Fig. 7f confirms the earlier hypotheses that particle formation occurs via a combination of atomisation and crystallisation in the outer and inner layers as well as agglomeration due to mixing of the two sections and due to coalescence at higher temperatures.

3.3.2. Wax 2 particle morphology via SEM

Greater variation in morphology was observed for Wax 2 particles. At low pressure and high temperature (100 bar/90 °C), particles tend to be spherical with smoother surfaces (Fig. 8a & b).

At these conditions, complete cooling and solidification of particles are delayed during expansion due to the reduced Joule-Thompson effect and the higher heat transfer requirements for solidification of individual particles. This delay results in the formation of spherical particles due to

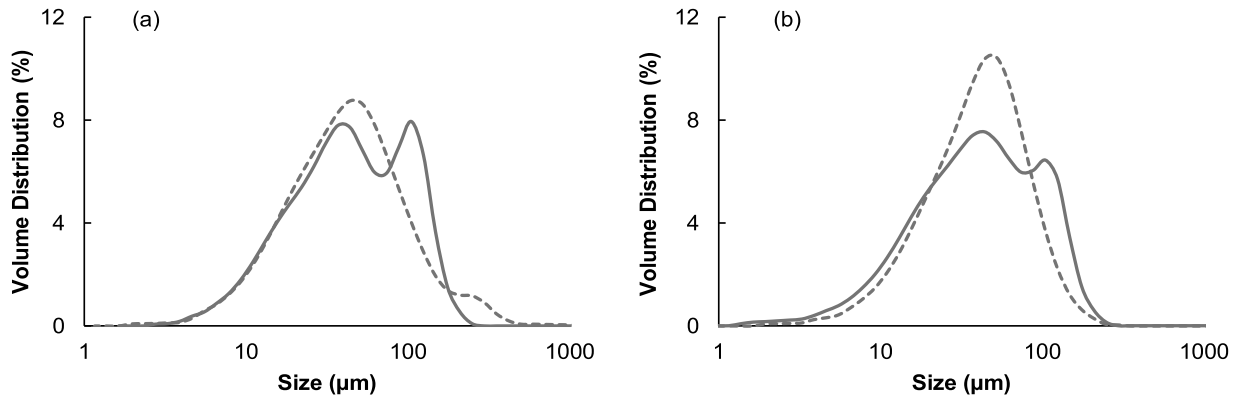

Fig. 4. PSDs of Wax 2 particles produced with Nozzle 2 at (a) 100 bar/ 70 °C (solid line) at 300 bar/70 °C (dashed line), and at (b) 100 bar/80 °C (solid line) and 300 bar/80 °C (dashed line), x_{wax_high}.

Table 6
Comparison of peak values of bimodal and unimodal distributions displayed by Wax 2 particles produced by Nozzle 2 and Nozzle 3 at x_{wax_low} and x_{wax_high}.

	P (bar)	T (°C)	x_{wax_low}				x_{wax_high}			
			1st Peak (μm)	Vol (x/x)	2nd Peak (μm)	Vol (x/x)	1st Peak (μm)	Vol (x/x)	2nd Peak (μm)	Vol (x/x)
Nozzle 2	100	60	32	1	-	-	86	0.37	26	0.63
		70	33	1	-	-	89	0.39	26	0.61
		80	46	1	-	-	95	0.30	27	0.70
	200	80	43	1	-	-	222	0.06	33	0.94
	300	60	47	1	-	-	108	0.53	38	0.47
Nozzle 3	100	70	28	1	-	-	87	0.37	26	0.63
		80	Not determined				89	0.40	26	0.60
		90	Not determined				272	0.08	29	0.92
	200	90	37	1	-	-	89	0.39	25	0.61
	300	80	227	0.06	40	0.94	37	1	-	-
		90	288	0.09	35	0.91	38	1	-	-

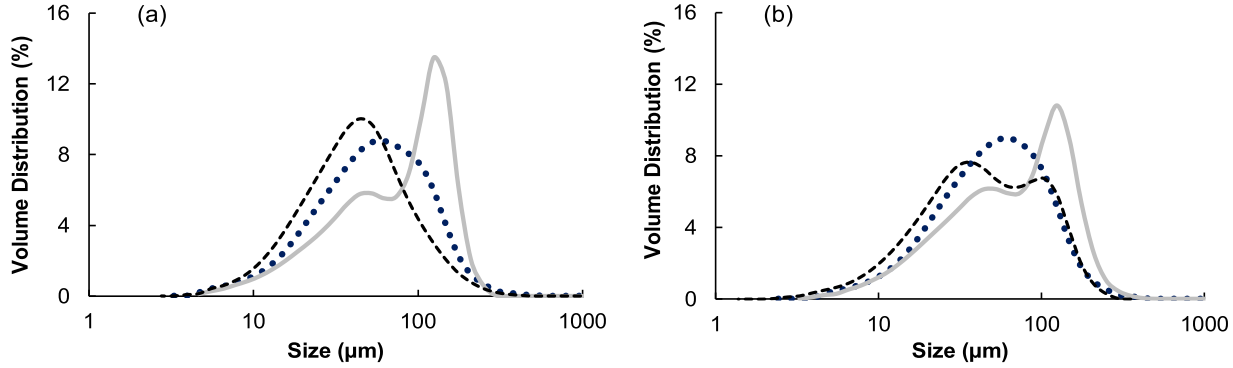

Fig. 5. Comparison of Wax 1 PSDs produced by Nozzle 1 (dotted line), Nozzle 2 (solid line) and Nozzle 3 (dashed line) at x_{wax_high} at a) 150 bar/40 °C and b) 150 bar/50 °C.

viscoelastic effects and minimisation of surface tension [3,22,38]. Due to the lower amounts of CO_2 dissolved/dispersed at lower pressures, these spherical particles are generally non-porous [33]. At higher temperatures, viscosity is reduced, and at higher pressures more CO_2 is present in the wax melt (despite the reduced density of CO_2 at elevated temperatures). More irregularly shaped and porous structures are thus formed due to reduced viscosity of the wax melt allowing for the increased CO_2 content to escape during expansion, resulting in rupturing of the particles (Fig. 8c). As with Wax 1 particles, SEM images of Wax 2 particles included the presence of flatter structures across processing conditions and different nozzles (see Fig. 8d), indicating that crystallisation as well as atomisation occurs during spraying.

3.3.3. *Dynamic image analysis of particle morphology*

The quantitative shape analyses (as provided by the dynamic imaging capabilities of the laser diffraction equipment) of Wax 1 particles measured median values of circularity ranging between 0.75 and 0.80, 0.56–0.62 median WL ratio, and 0.32–0.35 median transparency, where a value of 0 is equal to a completely opaque particle. Wax 2 particles were generally consistently more spherical, and slightly less transparent, with median circularity across the three nozzles varying only between 0.85 and 0.87, median WL ratio between 0.62 and 0.70, and median

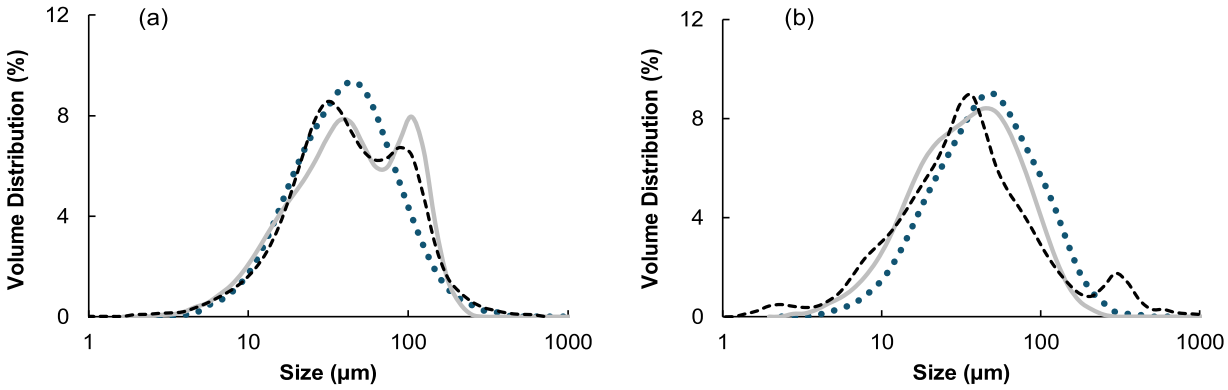

Fig. 6. Comparison of Wax 2 PSDs produced by Nozzle 1 (dotted line), Nozzle 2 (solid line) and Nozzle 3 (dashed line) at x_{wax_high} at a) 100 bar/70 °C and b) 100 bar/90 °C.

transparency between 0.31 and 0.34. This is due to the increased viscosity of Wax 2 versus Wax 1, resulting in greater resistance to droplet break-up during spraying and thus the formation of more spherical particles.

The shape parameters were not significantly impacted by changes in processing conditions or nozzle changes. For both waxes, the dynamic imaging results show that particles greater than 50 μm tend to be smoother and more opaque, while the shape parameters are more evenly distributed across particles size below 50 μm. This is in accordance with the theory that larger particles are formed in the inner solute rich layer passing through the nozzle. In this layer the CO_2 content is reduced, and hence rupturing of particles during micronisation occurs less frequently.

3.4. Bulk density

The bulk density of Wax 1 particles was not greatly impacted by changes in temperature and pressure, especially not at x_{wax_high}, as shown in Fig. 9. It was shown previously [31] that as wax mass fraction increases, the impact of temperature on density of the Wax + CO_2 mixture decreases. This is reflected in the bulk density results, with variation in bulk density per nozzle generally decreasing with an increase in wax loading due to the reduced variation in the amounts of CO_2 in the melts upon spraying.

At x_{wax_low}, bulk density is seemingly impacted more by particle size and PSD width rather than shape, similar to what was observed for rapeseed lipid particles prepared via PGSS [24]. This is corroborated by SEM imaging where definite differences in morphologies between particles prepared at different process conditions is not observed. Generally, a combination of smaller D50 and D90 values results in increased bulk density, likely due to improved packing density of distributions made up of smaller more homogeneous particles [24]. Exceptions are found where low mass yield and/or bimodal distributions were recorded.

When taking all the results into consideration for Wax 1, at x_{wax_low}, micronisation with Nozzle 2 at 45 °C and between 100 bar and 150 bar produces particles in high mass yield quantities with the best combination of smallest particle size, increased bulk density and high sphericity. When the wax loading is increased, Nozzle 1 produces particles with the best combination of small size, high bulk density and high yield at 200 bar/45 °C.

Where the bulk density of Wax 2 is concerned, the impact of pressure and temperature on bulk density is similar for all three nozzles, with bulk density increasing with temperature at 100 bar, with a decreased impact of pressure on bulk density at lower temperatures (Fig. 10). For both waxes, the tapped densities increased by a margin ranging between 5 % and 20 % of the corresponding bulk densities.

As temperature is increased at low pressure, particle solidification during expansion is delayed, resulting in the formation of spherical particles [3,22,38]. Due to the lower amounts of CO_2 dispersed/dissolved in Wax 2 at lower pressures, these spherical particles tend to be non-porous, as shown in Fig. 8(a and b), and thus display a high bulk density [33,39].

At low temperatures the high viscosity of the melt reduces the chances of CO_2 escape upon micronisation, resulting in the formation of cavities in the particles [33], with a subsequent reduction in bulk density. As temperature and pressure are increased viscosity decreases and the amount of CO_2 dissolved/dispersed in the melt increases, and it is expected that bulk density will decrease correspondingly [33,40]. Wax 2 bulk densities of particles produced at low temperature and pressure and at high temperature and pressure are however very similar, especially for Nozzles 1 and 2.

At low temperature, heat transfer requirements are low, and particle solidification is not delayed to a large degree. Solubility of CO_2 is limited and thus does not influence bulk density. As temperature is increased, the amount of heat to be transferred during particle solidification increases, and delayed particle solidification occurs, resulting in increased bulk densities. The reduction in bulk densities with increased pressure at high temperatures can partly be ascribed to greater quantities of CO_2 dispersed in the wax melt able to escape during atomisation due to reductions in viscosity, with particles as shown in Fig. 8c formed.

The solubility/dispersion of CO_2 in the wax melt is however not great enough to ensure that the majority of particles formed at these conditions are highly porous. The decrease in bulk density observed at high temperatures with increasing pressure can also be attributed to increased cooling experienced during particle formation, and thus particle solidification is not delayed to the same degree as at lower pressure. At 60 °C the heat transfer requirements are low enough for increases in pressure and thus greater cooling to not greatly impact particle formation.

The increased densities determined at 100 bar are recorded at conditions where much reduced mass yields were obtained, and thus it can be argued that these results are not truly representative. The trends are however also observed for Nozzle 1, where high mass yields were produced at corresponding conditions. Reduced mass yield possibly enhances the effect, with high bulk density particles disproportionally present in the fraction of free-flowing powder produced.

Nozzle 1 generally produces particles with the lowest bulk densities, with the largest bulk densities produced with Nozzle 2. This is due to the increased fluid velocity through the smaller Nozzle 1 reducing time available for particle growth and delayed particle solidification. The slower fluid velocity through Nozzle 2, combined with the tapered shape of the nozzle outlet results in slower particle solidification as well as greater agglomeration, thus bulk density is increased. The size, shape and bulk density results support the conclusion that Wax 2 particle formation is mostly governed by variation in temperature, via the impact on wax melt viscosity and the domination of heat transfer requirements over the impact pressure via CO_2 solubility during particle

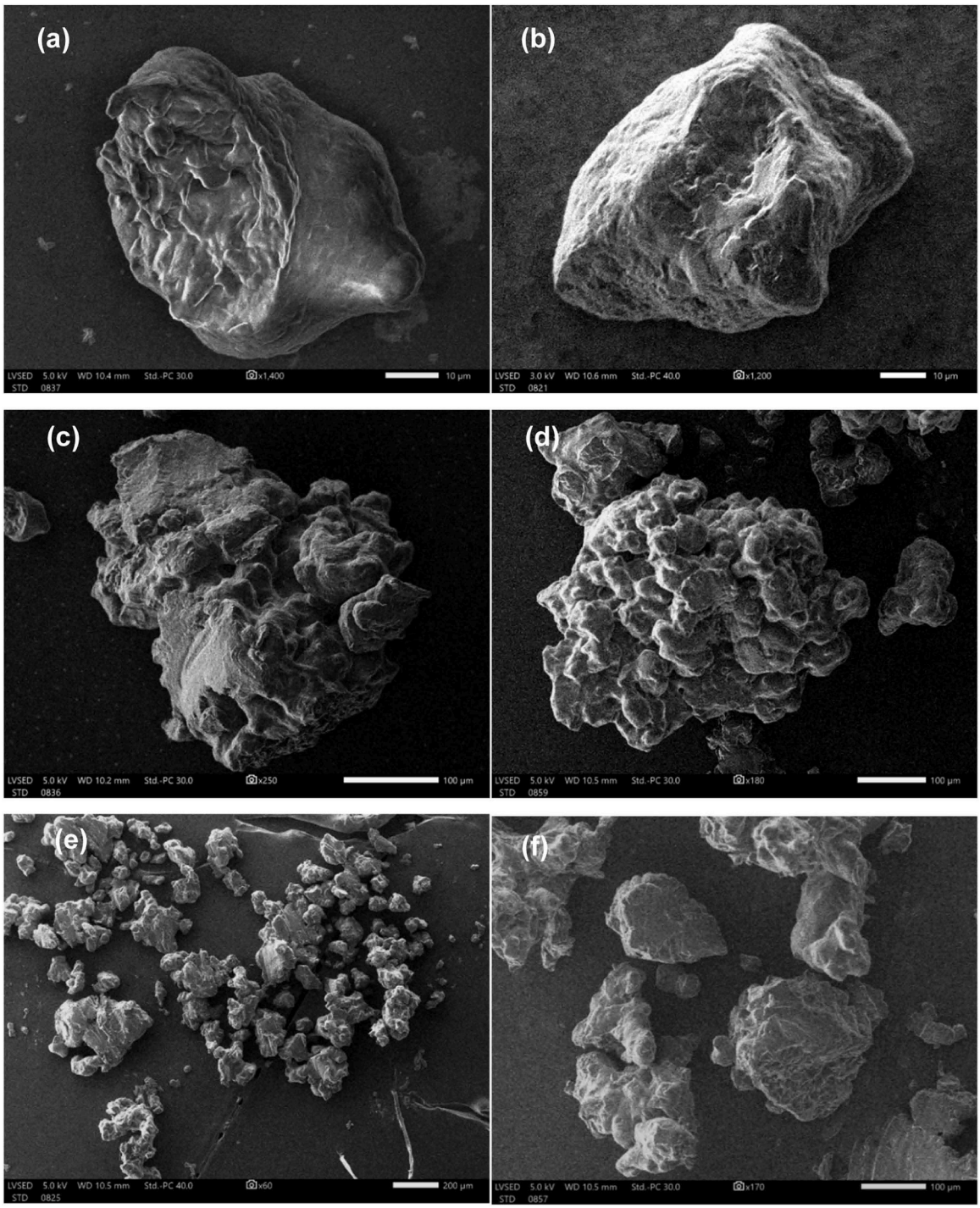

Fig. 7. SEM images of Wax 1 particles prepared at 200 bar/50 °C (a & c), 150 bar/45 °C (b & e) and at 150 bar/40 °C (d & f), showing relatively spherical individual particles (a and b), as well as larger structures with some porosity present (c and d) and flatter structures indicating crystallisation as method of particle formation (e and f).

solidification.

In conclusion, at x_{wax_low}, Nozzle 1 produces the smallest Wax 2 particles between 200 bar and 300 bar and 80 °C and 90 °C in high mass yields, but with reduced bulk density. Wax 2 particles with defined characteristics can be consistently produced in this operating range with limited variation in PSD parameters and bulk density. Reducing pressure to 100 bar/80 °C results in an almost doubling of bulk density at the cost of a 3 μm to 5 μm increase in median particle size. When wax loading is increased Nozzle 2 produces the smallest particles with increased bulk density in high yields between 200 bar and 300 bar at 90 °C.

3.5. Crystal structure and thermal analyses

The X-ray diffraction patterns of both waxes before micronisation display peaks with maxima between $2\theta = 21°$ and $2\theta = 24°$ (referred to as the high angle scattering region), as well as scattering below $2\theta = 10°$ (referred to as the low angle scattering region), as seen in Fig. 11 a (i) and b (i). The diffraction pattern of unprocessed Wax 1 is similar to patterns recorded for C28 crystals [41], an alkane that was shown previously [31] to be a good approximation for Wax 1 in terms of phase behaviour. Similarly, the diffraction pattern of unprocessed Wax 2

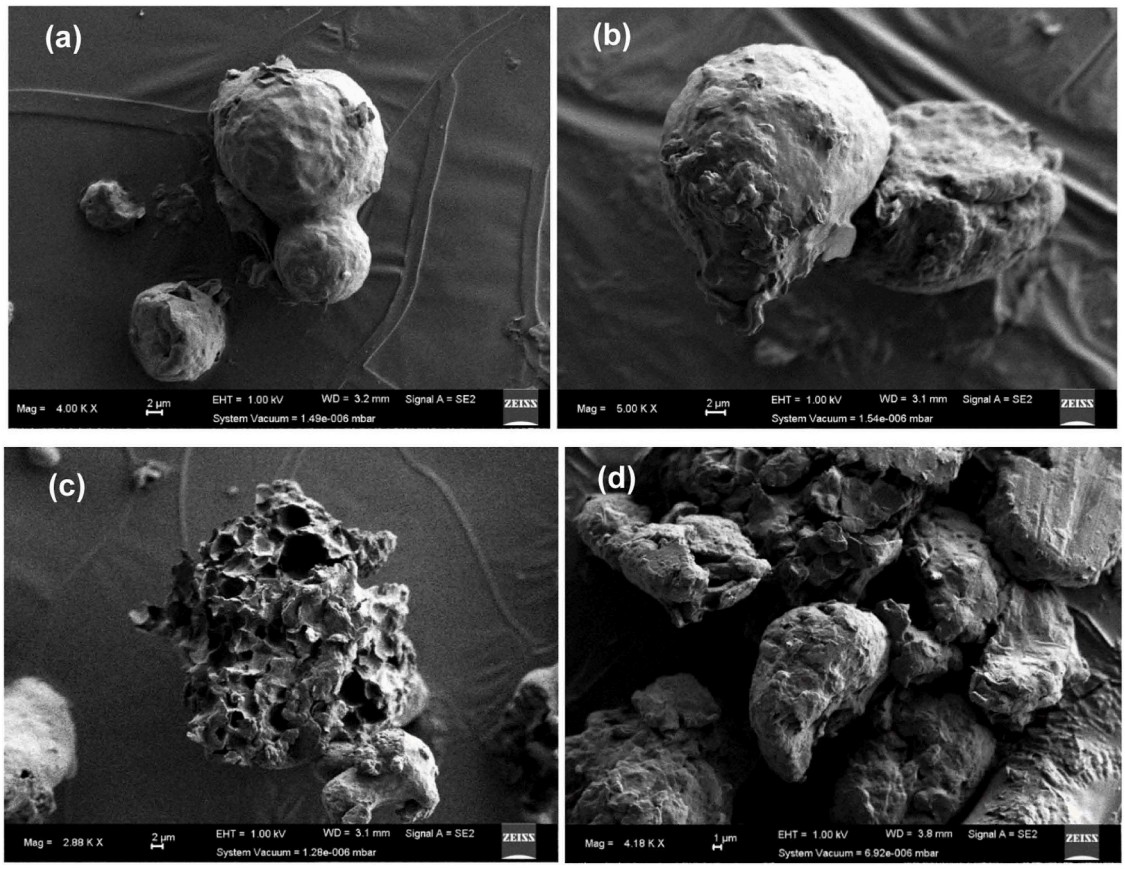

Fig. 8. SEM images of Wax 2 particles prepared at 100 bar/90 °C (a & b), at 300 bar/90 °C (c) and at (d) 100 bar/60 °C.

corresponds to those of melt grown crystals of the C32 and C36 alkanes [41]. The higher crystalline fraction of the higher T_m Wax 2 is reflected in the reduced amorphous halo at the base of the two high angle scattering peaks of Wax 2 versus Wax 1. Wax 2 samples also display reduced low angle scattering intensity relative to the accompanying high angle scattering intensity.

For both waxes micronisation generally resulted in a reduced lamellar structure, regardless of wax loading, processing conditions or nozzle diameter. This is indicated by the reduced intensity of the peaks in the low angle scattering region as compared to those in the high angle region, regardless of nozzle used. This reduction is due to incomplete reorganisation of chains and growth of the lamellar structure during rapid cooling upon spraying. As platelet size decreases, high angle scattering becomes more prominent [41].

DSC analyses of both waxes indicate a slight decrease in T_m after micronisation. The average T_m of Wax 1 particles is reduced slightly from 40.4 °C to between 39.6 °C and 40.1 °C, similar to what was seen when micronising monostearate and tristearin [42] (see Table S1 in Supplementary Material). These decreases in T_m correlates with the reduction in low angle scattering intensity seen after micronisation (as opposed to the unprocessed wax), as lamellar thickness determines the T_m of a compound [43]. The T_m of unprocessed Wax 2, 59.1 °C, reduces to between 56.8 °C and 58.9 °C after micronisation (Table S2 in Supplementary Material).

After six months, all Wax 1 particles produced similar diffraction patterns, a stable orthorhombic form with low angle scattering intensity approaching/exceeding the intensity of the high angle scattering peak at $2\theta = 21°$. Nozzle 1 particles tend to show more stable structures with less variation in diffraction patterns over the 6 months period than Nozzle 2 and Nozzle 3 particles. This can be attributed to the greater shear imparted by Nozzle 1 (smaller diameter) during micronisation resulting in the formation of more stable structures [44,45].

The T_m of micronised Wax 1 particles increases slightly over time, for all three nozzles at both mass loads, as well as the associated ΔH_m values. Molecules migrate from higher energy regions, where greater chain length disparity exists, to regions where chain lengths match well, leading to a more stable structure overall [46]. This results in higher degrees of crystallinity. Increased crystallinity might also be due to growth of crystallites with elimination of very small crystallites [46]. The changes in XRD structures, crystallite size and thermal parameters over time indicated that some changes in the crystal structure of Wax 1 particles occurred, most likely due to chain migration and secondary crystallisation.

The diffraction patterns of Wax 2 particles over a 6 month time indicated very little change in the crystal structure of the particles. Thermal analyses also indicated stable crystal structures with little change in T_m and ΔH_m. Greater changes were observed over time in the diffraction patterns of Wax 1 as compared to those of Wax 2. This could be ascribed to the improved mobility of the shorter chains of Wax 1 resulting in greater chain migration and/or secondary crystallisation.

4. Conclusions

The aim of this study was to successfully micronise FT waxes of differing T_m via PGSS, and to determine the impact of process conditions (temperature, pressure, loading and nozzle size) on particle size and shape. The impact of micronisation on the crystal structure of the wax particles was also investigated.

PGSS micronisation of Wax 1 and Wax 2 could be performed successfully. Processing conditions where optimum mass yields of free-flowing wax particles could be obtained were identified. The optimal operating region of Wax 1 was restricted by the pressure induced crystallisation observed previously and the high viscosity of the wax melt at low temperatures.

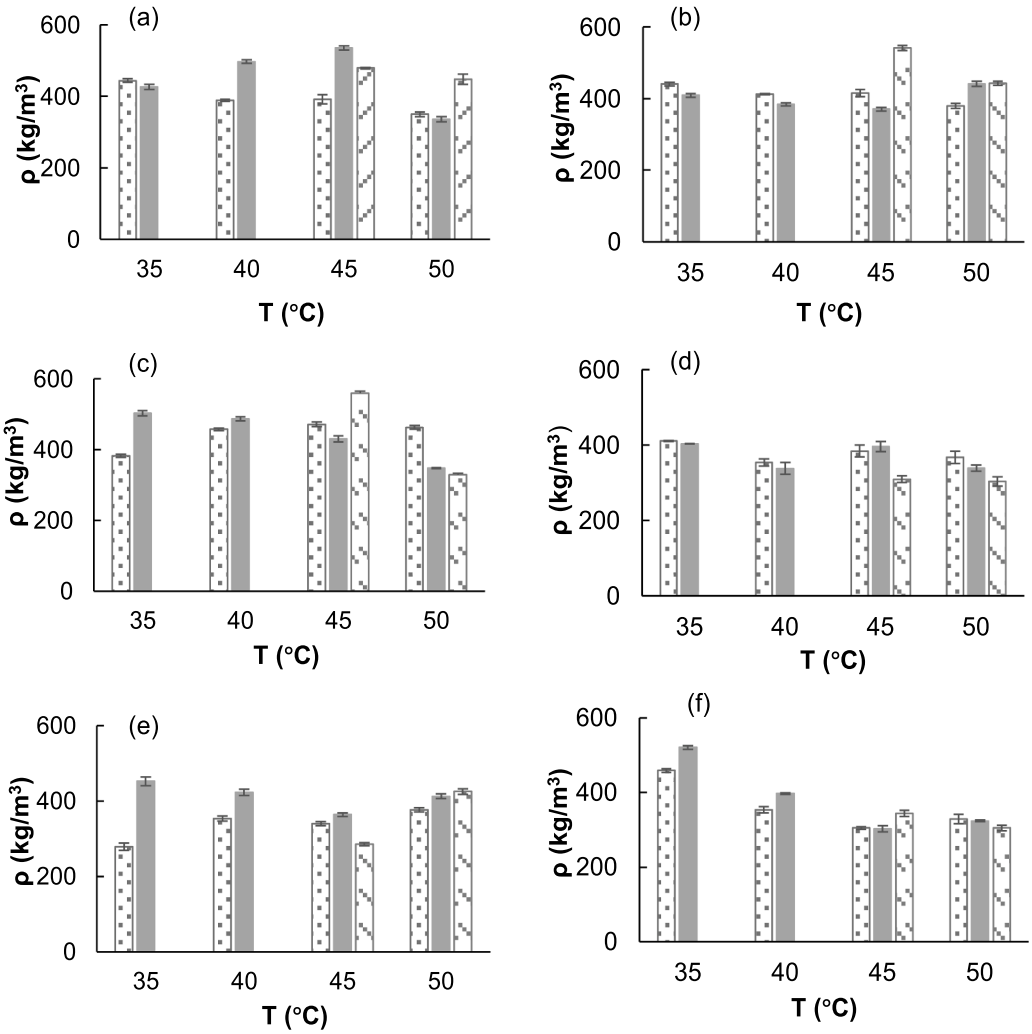

Fig. 9. Bulk density of Wax 1 particles prepared with Nozzle 1 at (a) x_{wax_low} and (b) x_{wax_high}, with Nozzle 2 at (c) x_{wax_low} and (d) x_{wax_high} and with Nozzle 3 at (e) at x_{wax_low} and (f) x_{wax_high} at 100 bar (dotted filled bars), at 150 bar (solid filled bars) and at 200 bar (slash filled bars).

Particle size and distributions shape was influenced by wax loading, temperature, pressure and nozzle diameter. Wax loading impacted particle formation via viscosity for both waxes, with increased wax loading resulting in increased viscosity, and thus more ineffective rupturing of the wax melts. Increased wax loading also contributed to the formation of bimodal particle size distributions. At high wax loading CO_2 content is reduced, resulting in limited expansion of the CO_2 richer outer layer of the wax melt in the nozzle during spraying. As a result, separate sets of particles were formed due to smaller particles originating from atomisation of the CO_2-rich outer layer and larger particles from the crystallisation of the wax-rich inner layer.

Temperature also impacted particle size via changes in viscosity as well as determining the degree of agglomeration, with increased temperature and reduced viscosity resulting in decreases in particle size. Improved rupturing of especially the inner layer of the wax melt resulted in reduced bimodality via consolidation of the particle sizes of the inner and outer material layers. These decreases were however offset by increased agglomeration at higher experimental temperature conditions.

Increased pressure resulted in greater CO_2 content, and thus improved cooling during expansion, with the impact of temperature on particle size mitigated. Increased pressure also resulted in increased expansion and mixing of the two material layers, leading to bimodal distributions becoming unimodal. Particle size was impacted more by nozzle shape than nozzle diameter. The use of a tapered nozzle resulted in increased agglomeration, and thus increased particle size, especially for Wax 1 with its increased liquid hydrocarbon fraction.

Particle shape was not quantifiably impacted by changes in processing conditions, especially in the case of Wax 1 where operating pressure could not be varied as greatly as for Wax 2. The presence of crystallite structures as well as spherical particles observed in SEM images of both waxes confirmed particle formation via these different mechanisms.

The biggest variation in bulk density was found with Wax 2, where high temperature and low pressure resulted in the formation of highly spherical solid particles which in turn resulted in a significant increase in bulk density. Otherwise, bulk density was not greatly impacted by changes in temperature and pressure, for both Wax 2 as well as Wax 1.

PGSS micronisation resulted in reduced lamellar structures observed for both Wax 1 and Wax 2 as opposed to the unprocessed waxes. Secondary crystallisation or chain migration occurred over time for both waxes, less so for Wax 2 than Wax 1 due to the greater chain mobility of the lower T_m Wax 1.

These results demonstrate the viability of PGSS micronisation of FT waxes, even with limited CO_2 sorption. The relationships between process parameters and resulting particle characteristics produced by a batch PGSS system are elucidated via the combination of data on median particle size, PSD, morphology, bulk density and crystal structure. Further optimisation of the experimental procedure may result in more stable flow during micronisation to better determine the impact of flow

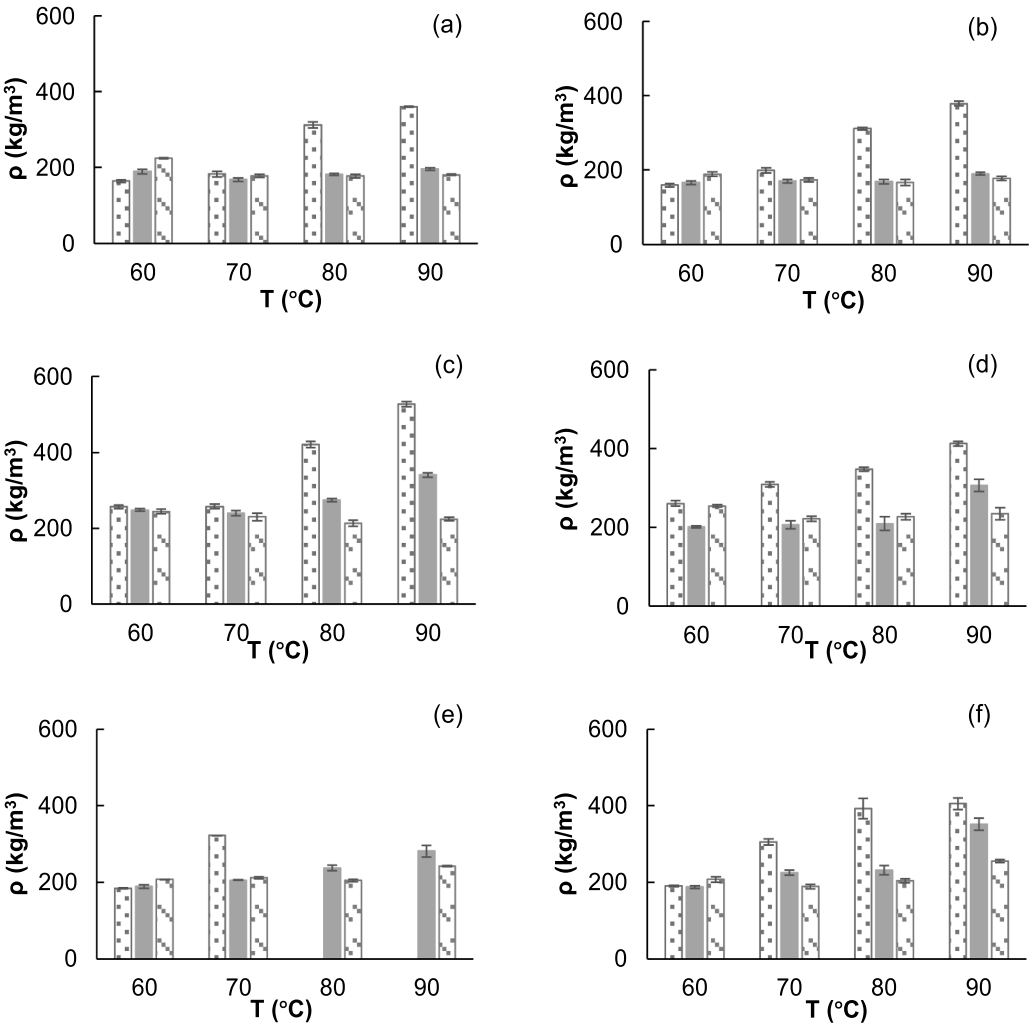

Fig. 10. Bulk density of Wax 2 particles prepared with Nozzle 1 at (a) x_{wax_low} and (b) x_2, with Nozzle 2 at (c) x_{wax_low} and (d) x_{wax_high} and with Nozzle 3 at (e) at x_{wax_low} and (f) x_{wax_high} at 100 bar (dotted filled bars), at 200 bar (solid filled bars) and at 300 bar (slash filled bars).

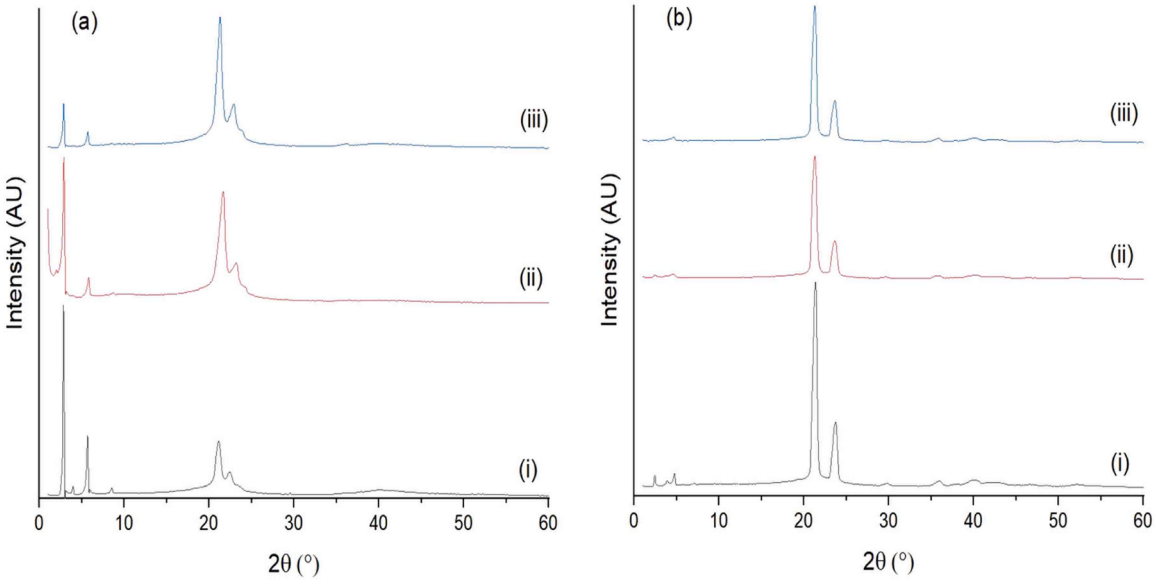

Fig. 11. Comparison of the XRD spectra of (a) Wax 1 (i) unprocessed, and micronised with Nozzle 1 at (ii) 150 bar/40 °C x_{wax_low} and (ii) at 150 bar/40 °C x_{wax_high}, and (b) Wax 2 (i) unprocessed, and micronised with Nozzle 1 at (ii) 300 bar/90 °C x_{wax_low} and (ii) at 300 bar/90 °C x_{wax_high}.

patterns on particle size distribution and to reduce particle agglomeration.

CRediT authorship contribution statement

Schwarz Cara: Writing – review & editing, Supervision, Investigation, Conceptualization. **Philip W. Labuschagne:** Writing – review & editing, Supervision, Project administration, Conceptualization. **Andri Swanepoel:** Writing – original draft, Validation, Project administration, Methodology, Investigation, Formal analysis, Data curation, Conceptualization.

Declaration of Competing Interest

The authors declare that they have no known competing financial interests or personal relationships that could have appeared to influence the work reported in this paper.

Acknowledgements

The authors would like to thank Dr James Wesley Smith and Ms Sharon Eggers for their assistance in imaging of the particles. The authors would also like to thank Prof Ray Suprakas, the Council for Scientific and Industrial Research and the Department of Science, Technology and Innovation (DST/CON 0052/2020) for funding of this work.

Appendix A. Supporting information

Supplementary data associated with this article can be found in the online version at doi:10.1016/j.supflu.2025.106785.

Data Availability

All data are available in the manuscript.

References

[1] Ž. Knez, M. Knez Hrnčič, M. Škerget, Particle formation and product formulation using supercritical fluids, Annu. Rev. Chem. Biomol. Eng. 6 (2015) 379–407, https://doi.org/10.1146/annurev-chembioeng-061114-123317.
[2] V.S. Carvalho, A.L.B. Dias, K.P. Rodrigues, T. Hatami, L.H.I. Mei, J. Martínez, J. Viganó, Supercritical fluid adsorption of natural extracts: technical, practical, and theoretical aspects, J. CO_2 Util. 56 (2022) 101865, https://doi.org/10.1016/J.JCOU.2021.101865.
[3] S.P. Nalawade, F. Picchioni, L.P.B.M. Janssen, Supercritical carbon dioxide as a Green solvent for processing polymer melts: processing aspects and applications, Prog. Polym. Sci. 31 (2006) 19–43, https://doi.org/10.1016/j.progpolymsci.2005.08.002.
[4] K.A. Kravanja, M. Finšgar, Ž. Knez, M. Knez Marevci, Supercritical fluid technologies for the incorporation of synthetic and natural active compounds into materials for drug formulation and delivery, Pharmaceutics 14 (2022) 1670, https://doi.org/10.3390/pharmaceutics14081670.
[5] A.V.M. Nunes, C.M.M. Duarte, Dense CO_2 as a solute, Co-Solute or Co-Solvent in particle formation processes: a review, Materials (2011) 2017–2041, https://doi.org/10.3390/ma4112017.
[6] E. Weidner, Ž. Knez, Z. Novak, Eur. Pat. EP 0744 (992) (1995) 0744992.
[7] E. Weidner, High pressure micronisation for food applications, J. Supercrit. Fluids 47 (2009) 556–565, https://doi.org/10.1016/J.SUPFLU.2008.11.009.
[8] F. Temelli, Perspectives on the use of supercritical particle formation technologies for food ingredients, J. Supercrit. Fluids 134 (2018) 244–251, https://doi.org/10.1016/j.supflu.2017.11.010.
[9] W. Wang, L. Rao, X. Wu, Y. Wang, L. Zhao, X. Liao, Supercritical carbon dioxide applications in food processing, Food Eng. Rev. 13 (2021) 570–591, https://doi.org/10.1007/s12393-020-09270-9.
[10] E. Badens, Y. Masmoudi, A. Mouahid, C. Crampon, Current situation and perspectives in drug formulation by using supercritical fluid technology, J. Supercrit. Fluids 134 (2018) 274–283, https://doi.org/10.1016/j.supflu.2017.12.038.
[11] R. Campardelli, L. Baldino, E. Reverchon, Supercritical fluids applications in nanomedicine, J. Supercrit. Fluids 101 (2015) 193–214, https://doi.org/10.1016/J.SUPFLU.2015.01.030.
[12] S. Klettenhammer, G. Ferrentino, K. Morozova, M. Scampicchio, Novel technologies based on supercritical fluids for the encapsulation of food grade bioactive compounds, Foods 9 (2020) 1395, https://doi.org/10.3390/foods9101395.
[13] I. Ribeiro Dos Santos, J. Richard, B. Pech, C. Thies, J.P. Benoit, Microencapsulation of protein particles within lipids using a novel supercritical fluid process, Int. J. Pharm. 242 (2002) 69–78, https://doi.org/10.1016/S0378-5173(02)00149-7.
[14] R. Couto, V. Alvarez, F. Temelli, Encapsulation of vitamin B2 in solid lipid nanoparticles using supercritical CO_2, J. Supercrit. Fluids 120 (2017) 432–442, https://doi.org/10.1016/j.supflu.2016.05.036.
[15] J.O. Akolade, M. Balogun, A. Swanepoel, R.B. Ibrahim, A.A. Yusuf, P. Labuschagne, Microencapsulation of eucalyptol in polyethylene glycol and polycaprolactone using particles from gas-saturated solutions, RSC Adv. (2019), https://doi.org/10.1039/C9RA06419B.
[16] S. Varona, S. Kareth, Á. Martín, M.J. Cocero, Formulation of lavandin essential oil with biopolymers by PGSS for application as biocide in ecological agriculture, J. Supercrit. Fluids 54 (2010) 369–377, https://doi.org/10.1016/j.supflu.2010.05.019.
[17] J. Yang, O.N. Ciftci, Development of free-flowing peppermint essential oil-loaded hollow solid lipid micro- and nanoparticles via atomization with carbon dioxide, Food Res. Int. 87 (2016) 83–91, https://doi.org/10.1016/j.foodres.2016.06.022.
[18] A.S. Pedro, S. Dalla Villa, P. Caliceti, S.A.B. Vieira de Melo, E.C. Albuquerque, A. Bertucco, S. Salmaso, Curcumin-loaded solid lipid particles by PGSS technology, J. Supercrit. Fluids 107 (2016) 534–541, https://doi.org/10.1016/j.supflu.2015.07.010.
[19] S. Klettenhammer, G. Ferrentino, H.S. Zendehbad, K. Morozova, M. Scampicchio, Microencapsulation of linseed oil enriched with carrot pomace extracts using particles from gas saturated solutions (PGSS) process, J. Food Eng. 312 (2022) 110746, https://doi.org/10.1016/J.JFOODENG.2021.110746.
[20] J. Yang, O.N. Ciftci, Formation of hollow solid lipid micro- and nanoparticles using supercritical carbon dioxide, Food Bioprod. Process 98 (2016) 151–160, https://doi.org/10.1016/J.FBP.2016.01.004.
[21] O.N. Ciftci, F. Temelli, Formation of solid lipid microparticles from fully hydrogenated canola oil using supercritical carbon dioxide, J. Food Eng. 178 (2016) 137–144, https://doi.org/10.1016/J.JFOODENG.2016.01.014.
[22] T. Hatami, J. Yang, M.A.A. Meireles, O.N. Ciftci, Sensitivity analysis of the formation of hollow solid lipid micro- and nanoparticles from CO_2-saturated solution of fully hydrogenated soybean oil, Powder Technol. 435 (2024) 119189, https://doi.org/10.1016/J.POWTEC.2023.119189.
[23] J.H. Yun, H.Y. Lee, A.K.M. Asaduzzaman, B.S. Chun, Micronisation and characterization of squid lecithin/polyethylene glycol composite using particles from gas saturated solutions (PGSS) process, J. Ind. Eng. Chem. 19 (2013) 686–691, https://doi.org/10.1016/J.JIEC.2012.10.005.
[24] P. Münüklü, P.J. Jansens, Particle formation of an edible fat (rapeseed 70) using the supercritical melt micronisation (ScMM) process, J. Supercrit. Fluids 40 (2007) 433–442, https://doi.org/10.1016/J.SUPFLU.2006.07.015.
[25] A. de Klerk, Fischer–Tropsch process, Kirk. -Othmer Encycl. Chem. Technol. (2013) 1–20, https://doi.org/10.1002/0471238961.fiscdekl.a01.
[26] J. Van de Loosdrecht, F.G. Botes, I.M. Ciobica, A.C. Ferreira, P. Gibson, D. J. Moodley, A.M. Saib, J.L. Visagie, C.J. Weststrate, J.W. Niemantsverdriet, Fischer-Tropsch synthesis: catalysts and chemistry. in: Comprehensive Inorganic Chemistry II: From Elements to Applications, Elsevier, 2013, pp. 525–557.
[27] H. Gruber, L. Lindner, S. Arlt, A. Reichhold, R. Rauch, G. Weber, J. Trimbach, H. Hofbauer, A novel production route and process optimization of biomass-derived paraffin wax for pharmaceutical application, J. Clean. Prod. 275 (2020) 124135, https://doi.org/10.1016/j.jclepro.2020.124135.
[28] M. Marchese, S. Chesta, M. Santarelli, A. Lanzini, Techno-economic feasibility of a biomass-to-X plant: Fischer-Tropsch wax synthesis from digestate gasification, Energy 228 (2021) 120581, https://doi.org/10.1016/J.ENERGY.2021.120581.
[29] Koen, L., 2003. The micronisation of synthetic waxes, Master's dissertation, University of Stellenbosch 2003.
[30] G.J. Griscik, R.W. Rousseau, A.S. Teja, Crystallisation of n-octacosane by the rapid expansion of supercritical solutions, J. Cryst. Growth 155 (1995) 112–119, https://doi.org/10.1016/0022-0248(95)00197-2.
[31] A. Swanepoel, P.W. Labuschagne, C.E. Schwarz, Measurement of phase transition, density and viscosity of supercritical carbon dioxide-Fischer-Tropsch wax mixtures, J. Supercrit. Fluids 220 (2025) 106546, https://doi.org/10.1016/J.SUPFLU.2025.106546.
[32] P.W. Labuschagne, M.J. John, R.E. Sadiku, Investigation of the degree of homogeneity and hydrogen bonding in PEG/PVP blends prepared in supercritical CO_2: comparison with ethanol-cast blends and physical mixtures, J. Supercrit. Fluids 54 (2010) 81–88, https://doi.org/10.1016/J.SUPFLU.2010.03.012.
[33] P. Kappler, W. Leiner, M. Petermann, E. Weidner, Size and morphology of particles generated by spraying polymer-melts with carbon dioxide. In: Sixth International Symposium on Supercritical Fluids, Institut National Polytechnique de Lorraine, Versailles, 2003.
[34] G. Liliana, S. Varona, M.J.Cocero Alonso, Encapsulation of garlic essential oil by batch PGSS process, innov. Rom, Food Biotechnol. 9 (2011) 60–67.
[35] L. Wollenweber, S. Kareth, M. Petermann, Polymorphic transition of lipid particles obtained with the PGSS process for pharmaceutical applications, J. Supercrit. Fluids 132 (2018) 99–104, https://doi.org/10.1016/J.SUPFLU.2017.06.009.
[36] J. Li, M. Rodrigues, A. Paiva, H.A. Matos, E. Gomes de Azevedo, Modelling of the PGSS process by crystallisation and atomisation, AIChE J. 51 (2005) 2343–2357, https://doi.org/10.1002/aic.10478.
[37] E. Kiran, Y.L. Sen, High-pressure viscosity and density of n-alkanes, Int. J. Thermophys. 13 (1992) 411–442, https://doi.org/10.1007/BF00503880.
[38] S. Pollak, M. Petermann, S. Kareth, A. Kilzer, Manufacturing of pulverised nanocomposites—Dosing and dispersion of additives by the use of supercritical

carbon dioxide, J. Supercrit. Fluids 53 (2010) 137–141, https://doi.org/10.1016/J.SUPFLU.2009.11.015.
[39] Martins Pintado, A.C. 2020 Production of Microparticles of Wax Using PGSS-Particles from Gas Saturated Solutions Process, Master's dissertation, NOVA University of Lisbon.
[40] S.P. Nalawade, F. Picchioni, L.P.B.M. Janssen, Batch production of micron size particles from poly(ethylene glycol) using supercritical CO_2 as a processing solvent, Chem. Eng. Sci. 62 (2007) 1712–1720, https://doi.org/10.1016/J.CES.2006.04.034.
[41] L. Li, X. Guo, D.H. Adamson, B.A. Pethica, J.S. Huang, R.K. Prud'homme, Flow improvement of waxy oils by modulating long-chain paraffin crystallization with comb polymers: an observation by X-ray diffraction, Ind. Eng. Chem. Res. 50 (2011) 316–321, https://doi.org/10.1021/ie101575w.
[42] Z. Mandžuka, Ž. Knez, Influence of temperature and pressure during PGSS™ micronisation and storage time on degree of crystallinity and crystal forms of monostearate and tristearate, J. Supercrit. Fluids 45 (2008) 102–111, https://doi.org/10.1016/J.SUPFLU.2007.11.006.
[43] A. Keller, Y. Udagawa, Crystallisation of short aliphatic polymer chains. I. general chain-folding behaviour, J. Polym. Sc. Part A Polym. Phys. 10 (1972) 221–238.
[44] G. Mazzanti, S.E. Guthrie, E.B. Sirota, A.G. Marangoni, S.H.J. Idziak, Orientation and phase transitions of fat crystals under shear, Cryst. Growth Des. 3 (2003) 721–725, https://doi.org/10.1021/cg034048a.
[45] S. Sonwai, M.R. Mackley, The effect of shear on the crystallisation of cocoa butter, JAOCS 83 (2006) 583–596, https://doi.org/10.1007/s11746-006-1243-6.
[46] J. Retief, J.Le Roux, Crystallographic investigations of a paraffinic Fischer-Tropsch wax in relation to a theory of wax structure and behaviour, S. Afr. J. Sci. 79 (1983) 234–239.